Supporting Information

Spin-Polarized Charge Separation in In_2O_3 Hollow Spheres for Efficiently Boosting Photo-Driving CO_2 Hydrogenation

Dawei Liu, Zhengdao Li, Zhe Lu, Zhisheng Shi,* Yongcai Zhang, San Zhang, Lu Wang, Chunfeng Zhang, Zhigang Zou, Yong Zhou**

Section 1: Experimental Section

Synthesis of V-In_2O_3 hollow spheres：For the production of V-In_2O_3, a solution was prepared by dissolving 1.18 g of indium(III) trinitrate and 3.00 g of urea in 150 mL of ethanol (Commercial Alcohols). The mixture was stirred for 10 minutes at room temperature until a clear solution was obtained. The solution was ultimately transferred into a 200 ml Teflon-lined autoclave, then heated to a temperature of 180 °C at a rate of approximately 5 °C per minute, and kept at this temperature for a duration of 10 hours. The reactor underwent natural cooling until it reached the ambient temperature. The solid formed was isolated using centrifugation and subjected to multiple washes with deionized water and ethanol. Following many hours of air drying at 60 °C, the initial precursor was ultimately subjected to calcination at 400 °C for 100 minutes, resulting in the formation of V-In_2O_3.

Characterization of V-In_2O_3：The phase compositions of the samples were characterized by a Rigaku D/MAX-Ultima III diffractometer equipped with a Cu Kα radiation source (λ = 1.54056 Å). The X-ray source was operated at 30 kV and 200 mA. The phase identification was made by comparison to the Joint Committee on Powder Diffraction Standards (JCPDS).

The field emission scanning electron microscopy images were obtained on a ZEISS Gemini G500 scanning electron microscopy operating at 30 kV. Transmission electron microscopy (TEM) and high-resolution transmission electron microscope (HRTEM) images were observed on a Tecnai G2 F20S-TWIN TEM instrument.

The surface compositional and chemical states of catalysts were analyzed through X-ray photoelectron spectroscopy (XPS) using an PHI5000 VersaProbe spectrometer with an Al Kα X-ray source. The operating conditions were chosen as 15 kV and 27 A. The carbon C 1s at 284.8 eV was used for calibration.

The N_2 physical adsorption-desorption test can be used to analyze the specific surface area and pore structure. The test was confirmed on a Micromeritics TriStar 3000 instrument. The specific surface area was analyzed by the Brunauer-Emmett-Teller (BET) method. The pore structure was investigated by the Barrett-Joyner-Halenda (BJH) method.

The weight loss and heat changes of samples at different temperatures were investigated through thermogravimetry analysis (TGA). The samples were tested in a Netzsch TG 209 F3 thermogravimetric analyzer under air.

The EPR data were obtained on a EPR-EMXplus spectrometer. Magnetic measurements were performed by a superconducting quantum interference device (SQUID) magnetometer (MPMS, Quantum Design).

For femtosecond-resolved TA measurement, a Ti : sapphire regenerative amplifier (90 fs, 1 kHz, Libra, Coherent Inc.) was used for TA spectroscopy. An optical parametric amplifier (OperA Solo, Coherent Inc.) pumped by the regenerative amplifier was used to generate the pump beam at the wavelengths of 380 nm. And the probe beam is a broadband supercontinuum light source generated by focusing a small portion of the femtosecond laser beam onto either a 3 mm-thick sapphire plate for visible range. The TA signal was then analyzed by a silicon CCD (S11071, Hamamatsu) mounted on a monochromator (Acton 2358, Princeton Instrument) at 1 kHz enabled by a custom-built control board from Entwicklungsbuero Stresing.

In situ diffuse reflectance infrared Fourier transform (DRIFTS) was conducted to characterize the adsorbed species on the sample surface and further monitor the catalytic reaction process in real-time. The tests were performed on a Thermo Nicolet iS50 FTIR spectrometer with a high-precision mercury-cadmium-telluride (MCT) detector cooled by liquid nitrogen. Beyond an infrared spectrometer, the experimental system consists of a diffuse reflectance accessory (Praying Mantis, Harrick), a high-temperature cell (HVC, Harrick, equipped with CaF_2 windows), a gas system, and a heating and temperature control device. Before the in situ tests, the catalyst was purged under a flowing Ar atmosphere at 373 K for 3 h to remove possible impurity molecules. Then, the background spectrum under an Ar atmosphere at different temperatures was collected to subtract the interference of H_2O and CO_2 on the sample spectrum. The scanning resolution was 2 cm^{-1}, and the number of scans was 32 times.

Catalytic performance：The catalytic performance was obtained through a batch reactor (V=170 mL) with a silica viewport at the top. The reactor was purged with H_2 (50 kPa) and CO_2 (50 kPa) and loaded with 5 mg mass of catalysts at room temperature. (Specifically showed in **Fig. S16**, 5 mg sample was first spread on quartz wool film, the quartz wool film was secured to a 304 stainless steel holder, and the holder was placed in a batch reactor. The batch reactor was hermetically sealed and the gas was pumped out and injected sequentially with hydrogen at 50 kPa and carbon dioxide at 50 kPa.) The reaction was conducted for 1 h without external heating. A Xe light (bulb power is 50 W, measured light density is 1.4 W/cm^2 and wavelength range is 300~800 nm) was used for providing light irradiation from viewport. Products were analyzed with an online gas chromatograph (GC, Agilent 8890) equipped with a flame-ionized detector (FID). GC gave the amount of product (noted as A) in parts per million (ppm). The rate of product is given by Equation S2.

Measurements of the surface temperature of the samples were carried out in another batch reactor. Burying the tip of the thermocouple in the sample and control the distance between the outlet of the light source and the sample as in the above experiment, specifically showed in **Fig. S17**.

Section 2: Supplementary Figures, Tables & Equations

$$t = \frac{A_1\tau_1 + A_2\tau_2}{A_1 + A_2} \tag{S1}$$

A_1, A_2 are the two coefficients in the bi-exponential function.

$$rate(\mu mol\, h^{-1}\, g^{-1}) = \frac{V(L)}{22.4(L\, mol^{-1})\, mass(g)\, time(h)} \times A(ppm) \times 10^6 \tag{S2}$$

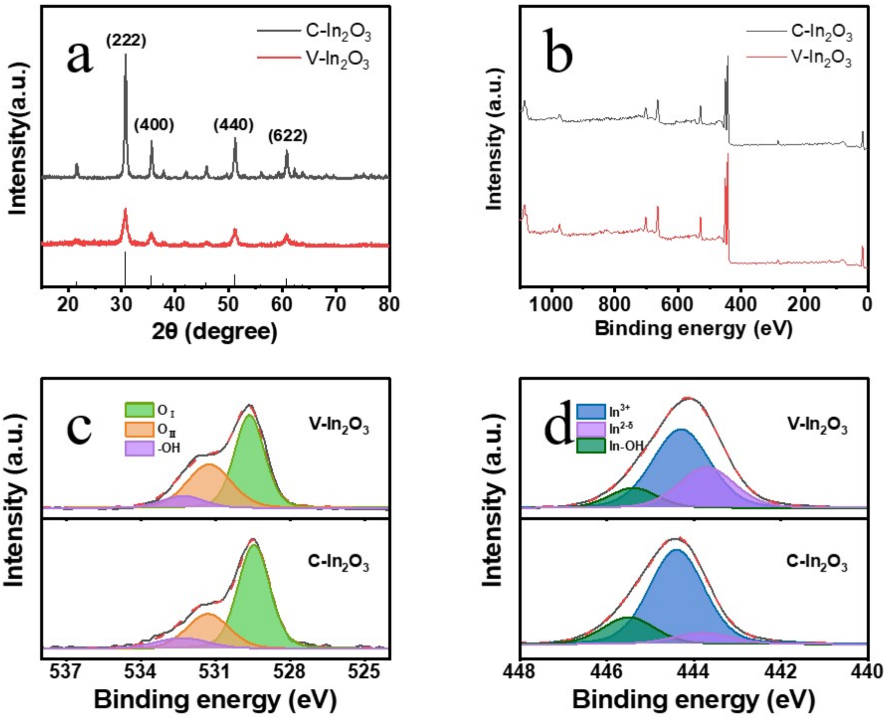

Fig. S1 (a) XRD patterns of C-In_2O_3 and V-In_2O_3, (b) XPS spectra of C-In_2O_3 and V-In_2O_3, (c) O 1s core level XPS spectra and (d) In $3d_{5/2}$ XPS spectra.

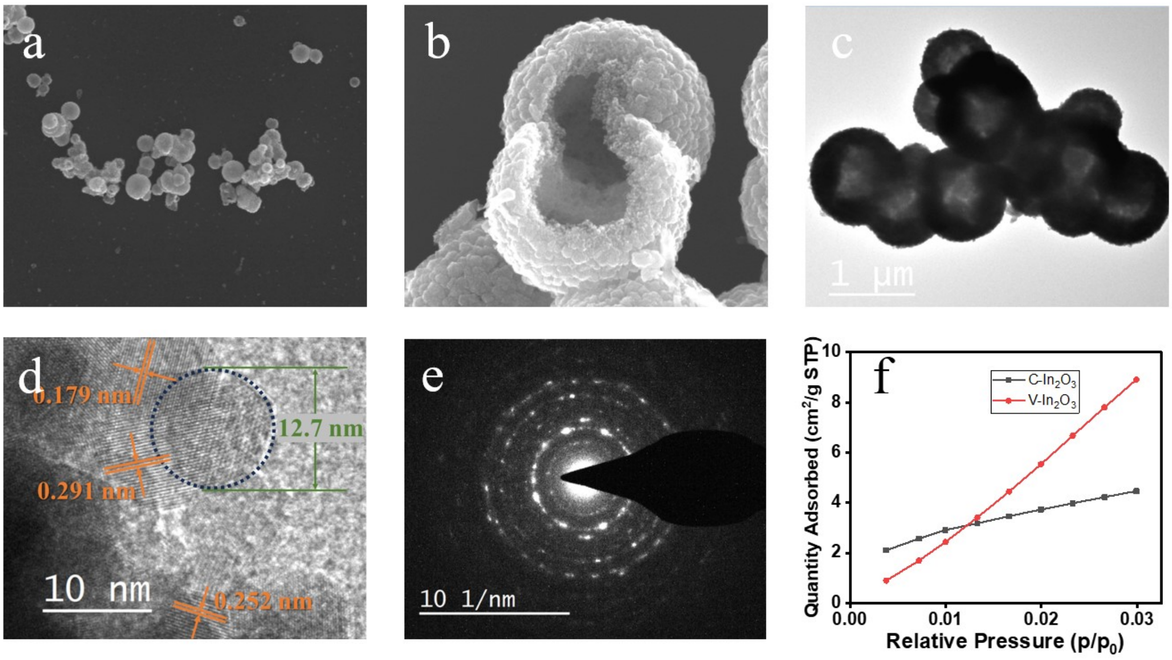

Fig. S2 (a, b) SEM images, (c) TEM image, (d) HRTEM image of V-In_2O_3 (e) corresponding SAED pattern and (f) CO_2 adsorption curve.

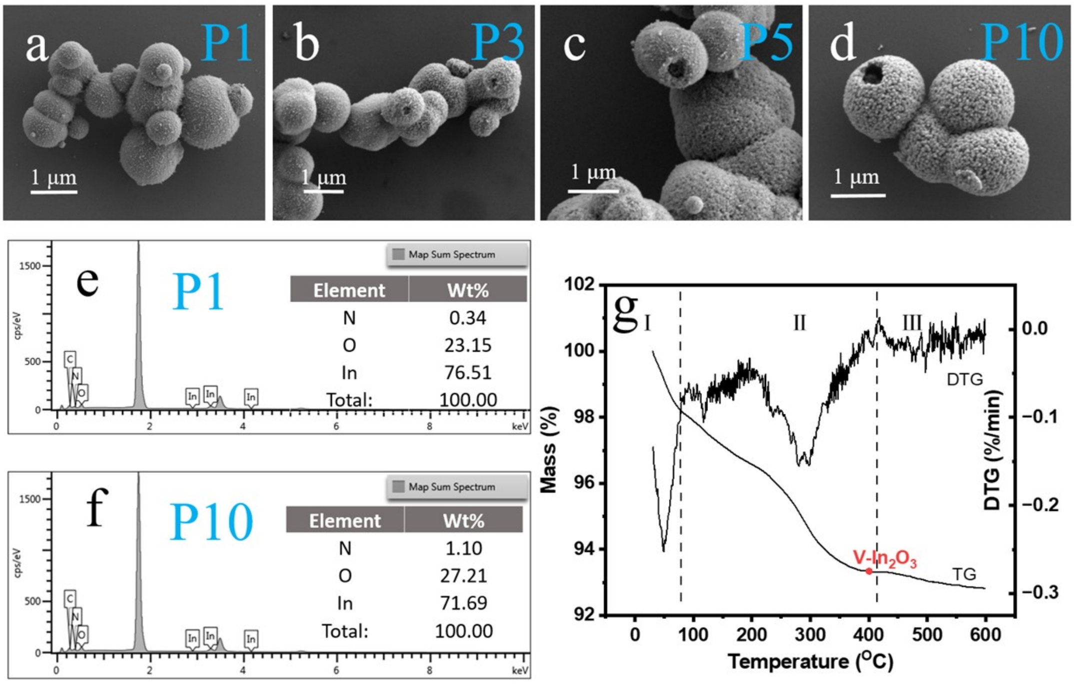

Element	Wt%
N	0.34
O	23.15
In	76.51
Total:	100.00

Element	Wt%
N	1.10
O	27.21
In	71.69
Total:	100.00

Fig. S3 (a)-(d) SEM images of precursor of 1h, 3h, 5h and 10h hydrothermal time. EDS pictures of (e)P1 and (f)P10. (g) TG spectrum of simulated synthetic process of precursor P10.

Our product, like Matuan, a traditional Chinese delicacy, goes through a process from solid to hollow. The SEM images (Fig. S3a-d) were obtained for precursors subjected to hydrothermal heating for 1 h, 3 h, 5 h, and 10 h, respectively. These precursors are referred to as P1, P3, P5, and P10. Observations reveal the formation of solid balls, ranging in size from approximately 0.2 to 1 μm, during the initial stages of the reaction (Fig. S3a). The pertinent reaction are as follows:[31,32]

$NH_2CONH_2 + C_2H_5OH \rightarrow C_2H_5OCONH_2 + NH_3$ (1)

$In^{3+} + 3\ NH_3 + 4\ C_2H_5OH \rightarrow InOOH + 3\ NH_4^+ + 2\ C_2H_5OC_2H_5$ (2)

Both urea and the carbamate produced in the reaction solution include many electronegative carbonyl groups (-CO-), which have a strong attraction for electropositive In^{3+} ions. Specifically, urea and carbamate serve as the reaction site for reaction 2. Therefore, the solid balls depicted in Fig. S3a should consist of a combination of InOOH and either urea or carbamate. The presence of the N element in P1 is confirmed by the Energy Dispersive Spectrometer (EDS) image (Figure S5e). Over time, the flaws in P3 and P5 become increasingly apparent. In P10, numerous balls, ranging in size from approximately 0.4 to 1.5 micrometers, exhibit obvious holes, while some specific balls have even developed well-defined hollow structures (Fig. S3d). There is a notable rise in the amount of nitrogen (N) in P10, with a concentration of 1.10 wt%, compared to P1, which has a concentration of 0.34 wt% (Fig. S3e, f). As well as the increase in surface nitrogen, the growth of the ball and hollow structure can be attributed to the diffusion of nitrogenous chemicals from the interior to the surface. The decomposition of urea results in the formation of ammonia and carbamate, which are nitrogenous compounds. The molar ratio of In to O elements of roughly 1:2 may aid in determining that the precursor is amorphous indium oxyhydroxide (InOOH).

The thermogravimetric (TG) analysis was conducted to replicate the synthetic process of V-In_2O_3 from hydrothermal precursors (Fig. S3g), as described earlier ($2InOOH \rightarrow In_2O_3 + H_2O$). The analysis revealed a decrease in weight of 7.1%, which closely aligns with the expected theoretical mass loss of 6.1%. The slight discrepancy can be attributed to the presence of nitrogenous substances and absorbed water. As shown in Fig. S3g, the mass change of the precursor could be divided into three processes throughout the temperature change. In process I (below 100 °C), mass loss dominated by adsorbate desorption. In process II (100 - 400 °C), the precursor undergoes a phase transition. At 300 °C, the sample was undergoing a transformation into $In_2O_{3-x}(OH)_y$ and experiencing a rapid loss of mass. At 400 °C, the transformation of the sample has essentially completed and numerous oxygen defects have formed, resulting in a stabilized mass and a modest increase in specific surface area. In process III (above 400 °C), the mass of the sample reduced somewhat once more. This was caused by the disappearance of the hydroxyl group in $In_2O_{3-x}(OH)_y$, transforming into In_2O_3, resulting in a light decrease in specific surface area. Ultra-high specific surface area of V-In_2O_3 offers a large number of active sites for PRWGS reaction, enabling high catalytic efficiency.

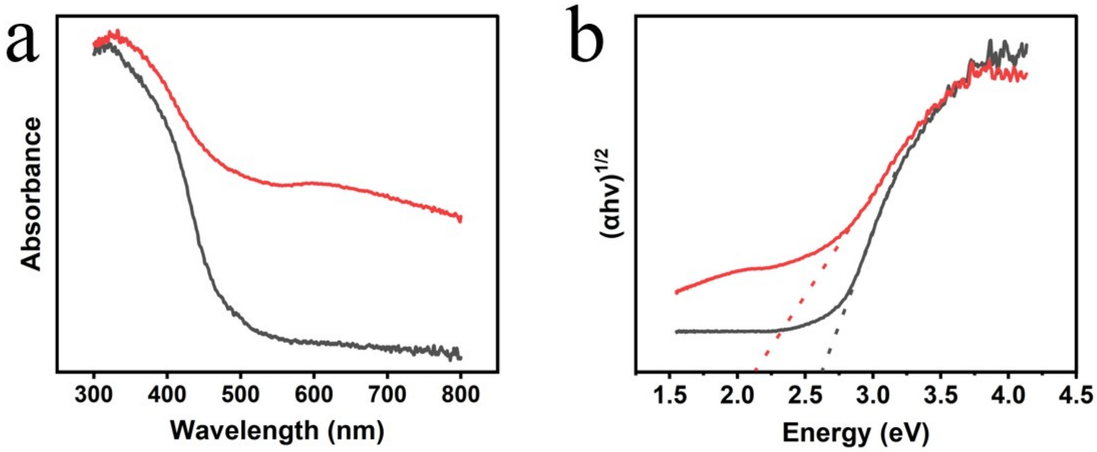

Fig. S4 (a) Optical absorption spectrum, (b) Tauc plot of Kubelka-Munk function for C-In_2O_3 (black) and V-In_2O_3 (red).

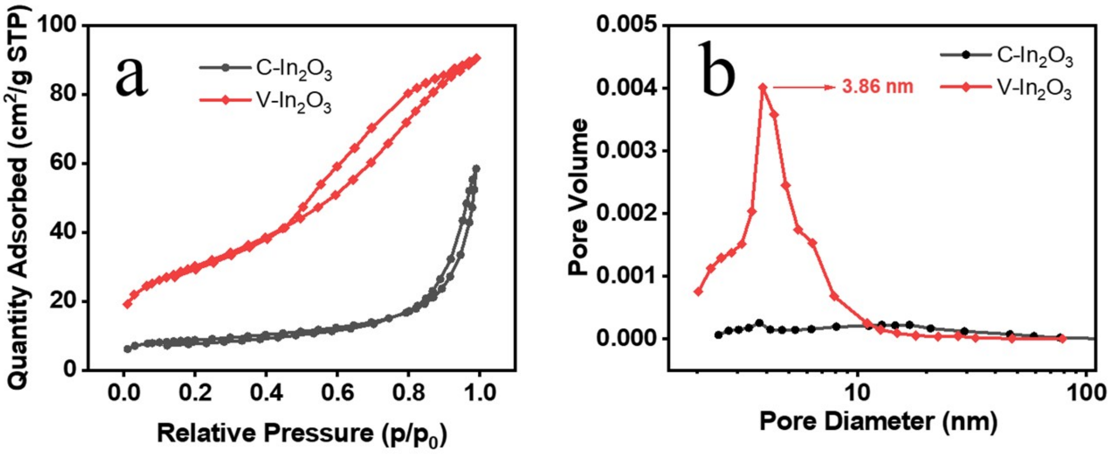

Fig. S5 (a) N_2 physisorption isotherms (adsorption-desorption branches). (b) Pore size distributions.

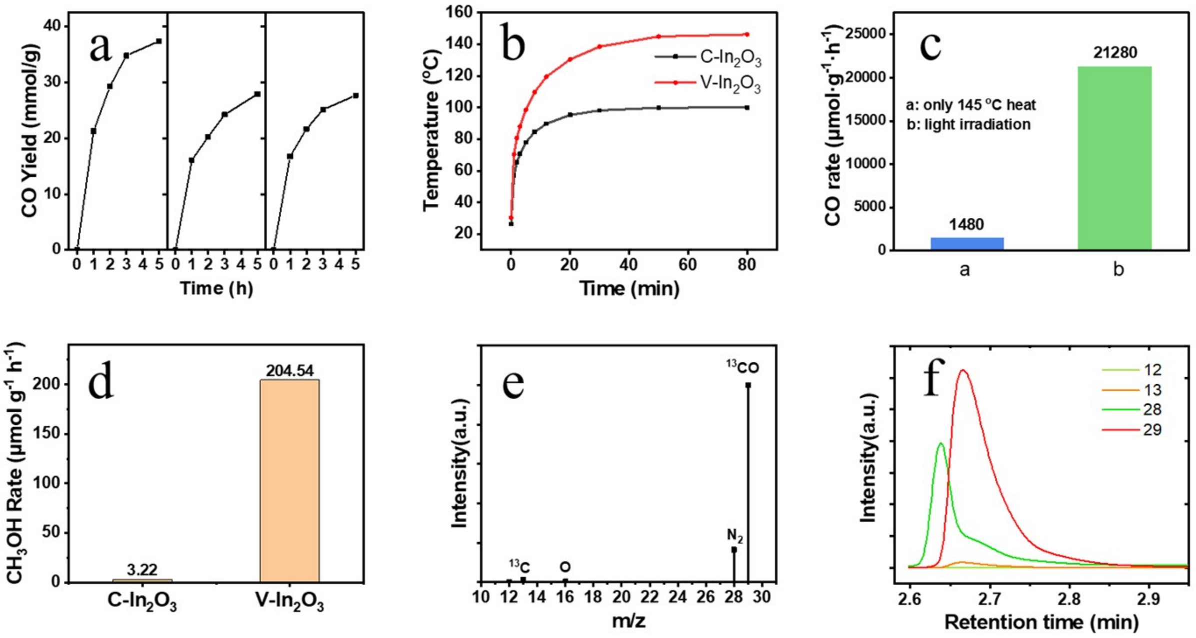

Fig. S6 (a) Catalytic stability testing of V-In$_2$O$_3$.[a] Condition: H$_2$: CO$_2$ = 50 : 50 kPa, light intensity = 1.4 W cm^{-2}, without external heating. After 5 hours of reaction, refill the batch reactor with fresh raw gas H$_2$: CO$_2$ = 50 : 50 kPa. (b) The temperature on the surface of C-In$_2$O$_3$ and V-In$_2$O$_3$, (c) Control experiment on V-In$_2$O$_3$ in the dark at 145 °C, (d) Photocatalytic CO$_2$ hydrogenation. Condition: H$_2$:CO$_2$ = 150:50 kPa, light intensity = 1.4 W cm^{-2}, without external heating and measurement time =1 h, and (e, f) Isotopically-labeled carbon tracing.[b]

[a] Some possible reasons for the decline of catalytic rate.

1. V-In$_2$O$_3$ possesses strong light-absorbing properties (Fig. S4), and the surface temperature can reach 145 ^{O}C under light illumination (Fig. S6b). At such a high temperature, the passivation effect of hydrogen on the surface will be very significant, and therefore the catalytic activity is irreversibly injured.

2. V-In$_2$O$_3$ has a strong adsorption capacity for CO$_2$ (Fig. S2f), but the reduction of adsorbed CO$_2$ to formate is slow, and CO$_2$ that has not yet been reduced continues to be embedded in the active site, reducing the number of active sites involved in the reaction and thus lowering the catalytic rate.

3. Although the surface of the sample can reach 145 degrees Celsius ^{O}C under light illumination (Fig. S6b), this temperature is still very low for the inverse water-gas shift (RWGS) reaction, and the catalytic efficiency of V-In$_2$O$_3$ is so high that it may have touched the equilibrium of the reaction at this temperature after one hour.

[b] The reason for the presence of N$_2$.

During the experiment, the needle of the gas extractor utilized for extracting the reaction gas was relatively long. Consequently, a certain amount of air inevitably remained within the needle. Given that air contains nitrogen, this could result in the contamination of the product with nitrogen, leading to the presence of nitrogen elements in the isotope-labeled carbon tracing results. Fig. S6e demonstrated that line 28 (attributed to N_2 or ^{12}CO) and 29 (attributed to ^{13}CO) exhibited distinct retention times, suggesting that line 28 did not correspond to a ^{12}CO signal.

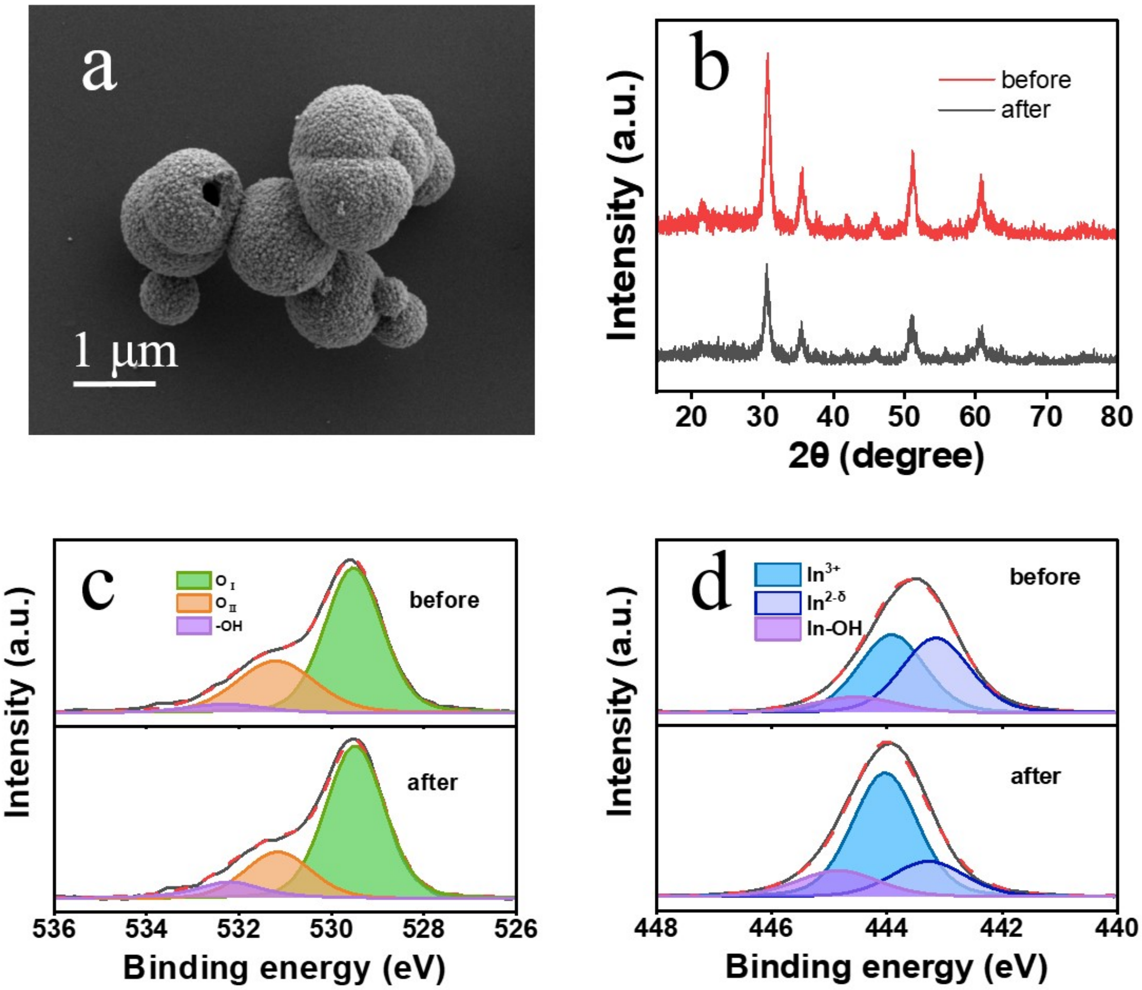

Fig. S7 (a) SEM, (b) XRD, (c) XPS O 1s and (d) XPS In $3d_{5/2}$ of V-In_2O_3 after photo-induced catalyst evaluation.

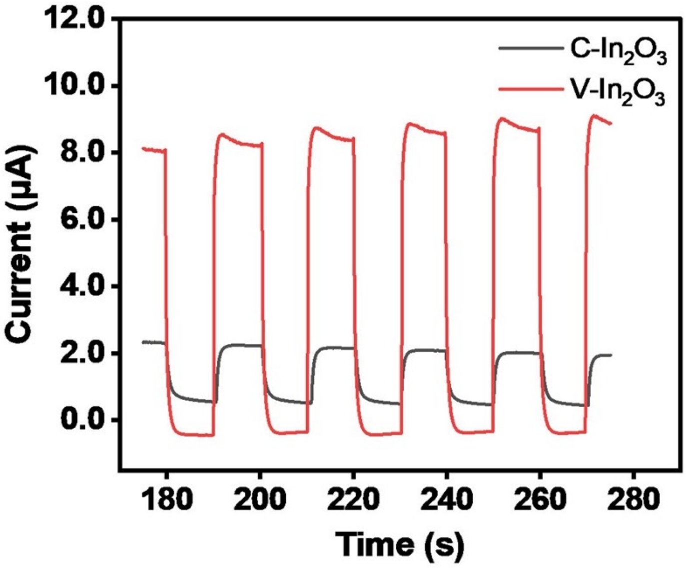

Fig. S8 Photocurrent measurements for C-In$_2$O$_3$ and V-In$_2$O$_3$.

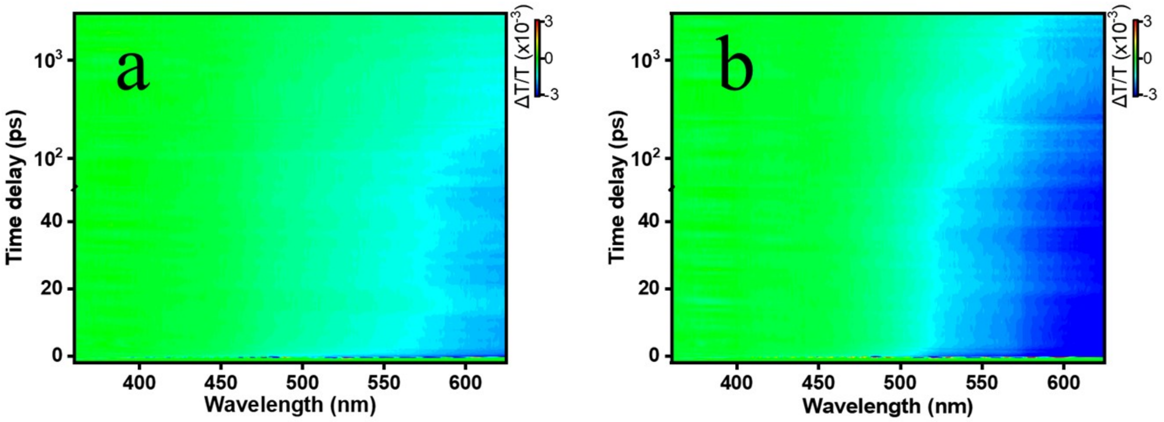

Fig. S9 TAS heat map of (a) C-In_2O_3 and (b) V-In_2O_3.

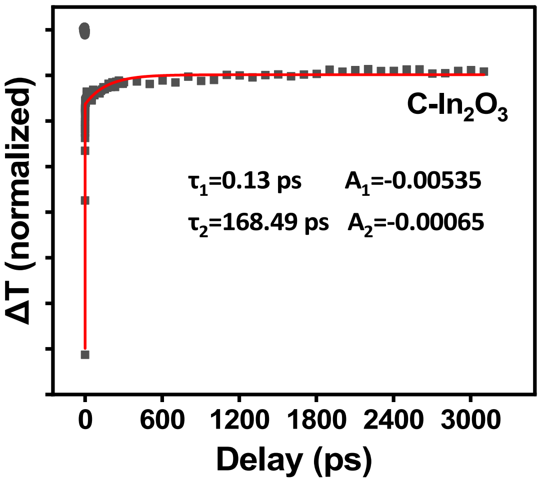

Fig. S10 TAS at 579 nm for C-In_2O_3.

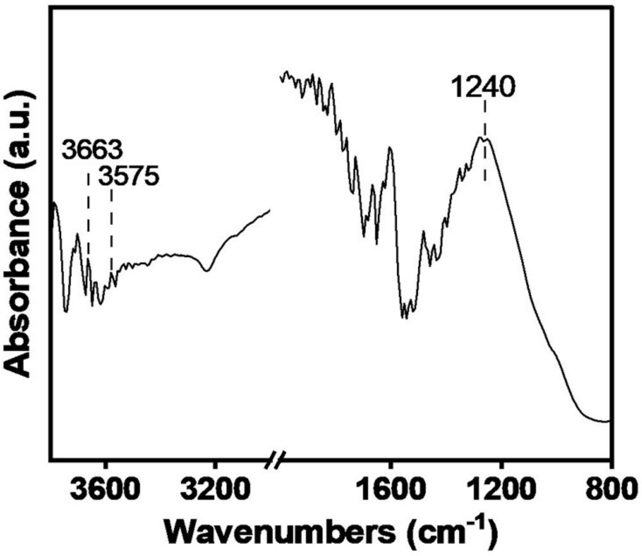

Fig. S11 In situ DRIFTS spectra of V-In_2O_3 obtained under Ar.

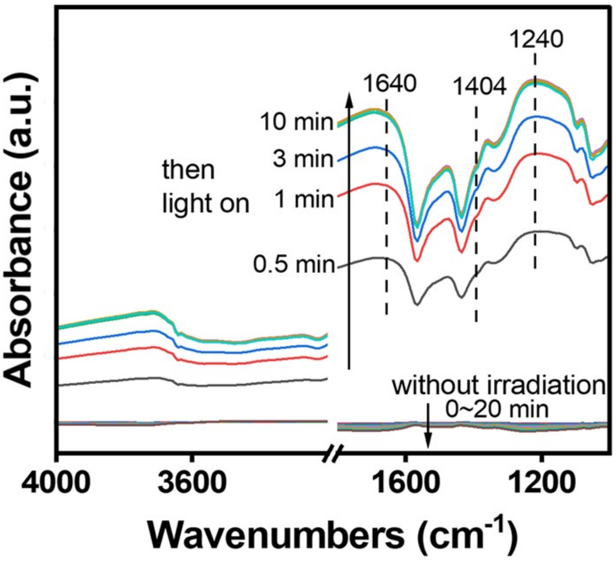

Fig. S12 In situ DRIFTS spectra of V-In_2O_3 obtained under H_2.

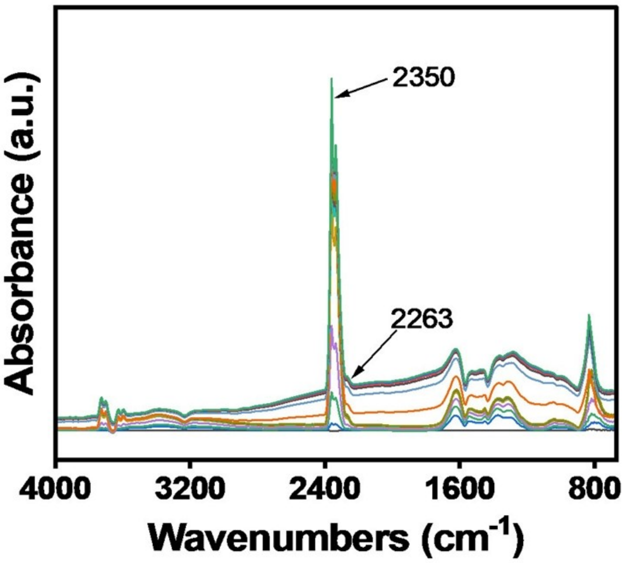

Fig. S13 In situ DRIFTS spectra of V-In_2O_3 obtained under H_2 and CO_2 (1:1).

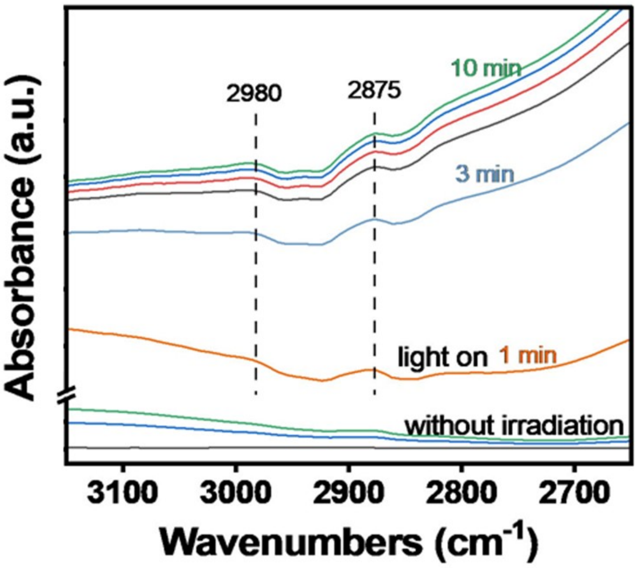

Fig. S14 In situ DRIFTS spectra of V-In_2O_3 obtained under H_2 and CO_2 (1:1).

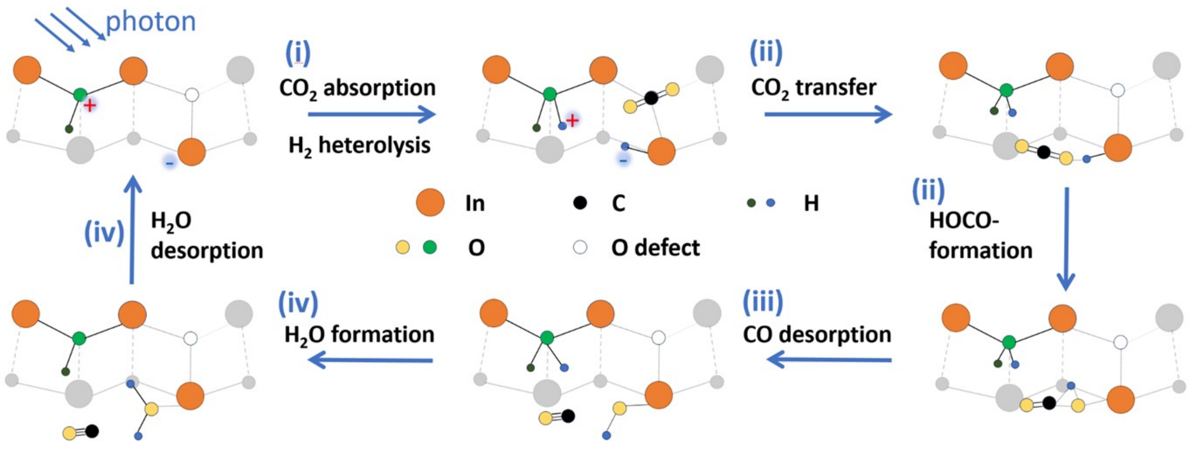

Fig. S15 Proposed catalytic reaction pathway.

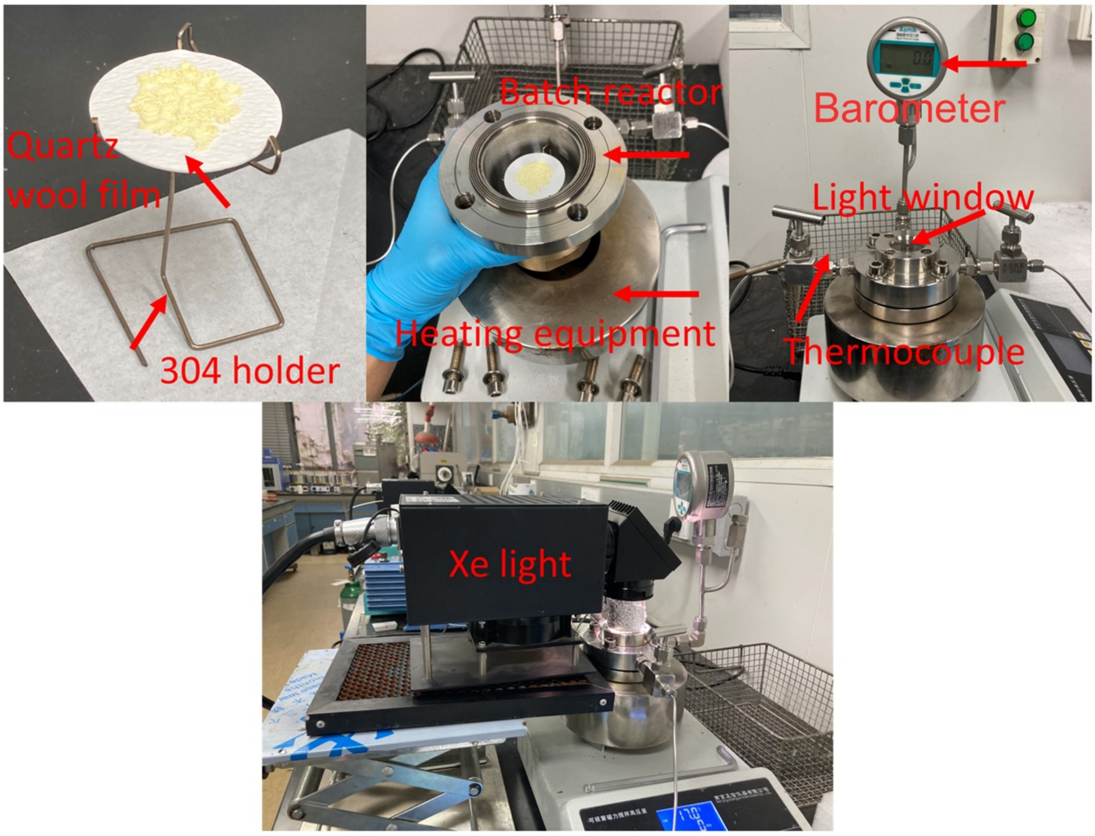

Fig. S16 Digital images of photocatalytic evaluation devices.

Fig. S17 Specific measurement of surface temperature of catalysts.

Tab. S1 Quantitative analysis for surface In and O from the XPS.

			C-In_2O_3		V-In_2O_3	
	Position	Assignment	FWHM[a]	Area %	FWHM	Area %
O 1s analysis	529.5 eV	In-O	1.5 eV	65.5%	1.4 eV	54.5%
	531.2 eV	[O]	1.9 eV	21.8%	1.9 eV	31.7%
	532.3 eV	-OH	2.0 eV	12.7%	1.8 eV	13.8%
In $3d_{5/2}$ analysis	444.1 eV	In^{3+}	1.5 eV	72.8%	1.5 eV	58.6%
	443.2 eV	$In^{2-\delta}$	1.6 eV	9.2%	1.5 eV	29.0%
	444.9 eV	In-OH	1.4 eV	18.0%	1.4 eV	12.4%
atomic ratio	[b]C		25.5%		21.4%	
	O		44.5%		46.8%	
	In		30.0%		31.8%	
	O/In ratio		1.483		1.471	

[a] FWHM: Full width of half maxima

[b] Carbon may originate from the absorbed CO_2 molecules or contamination.

Tab. S2 Summarized photothermal catalytic performance of In_2O_3-based materials for CO_2 hydrogenation.

	Catalyst	**Target product**	**Reactor type**	**Rate/ µmol g_{cat}^{-1} h^{-1}**	**Selectivity/%**	**Ambient reaction temperature/°C**	**H_2/CO_2**	**Pressure /bar**	**Reference**
Photothermal CO_2 to CO	In-Em In_2O_3	CO	Batch	8600	99.99	300	3	1.8	[1]
	$Bi_zIn_{2-z}O_{3-x}(OH)_y$ (z=0.03%)	CO	Batch	1.32	100	150	1	2.1	[2]
	$TiN@TiO_2@$ 19% $In_2O_{3-x}(OH)_y$	CO[b]	Flow	653.41[a]	100	225	3	1	[3]
	$In_2O_{3-x}(OH)_y$	CO	Flow	15	99[a]	150	1	1	[4]
	$In_2O_{3-x}(OH)_y$	CO	Flow	153	100	190	1	1	[5]
	$In_2O_{3-x}(OH)_y$ on Ni foam	CO	Flow	755	100	295	1	1	[6]
	$In_2O_{3-x}(OH)_y$	CO	Batch	1.38	100	150	1	2	[7]
	$In_2O_{3-x}(OH)_y$	CO	Batch	1.2	100	150	1	Not given	[8]
	$Bi_zIn_{2-z}O_{3-x}(OH)_y$ (z=0.05%)	CO	Batch	123.6	100	Not given	Not given	Not given	[9]
	V-In_2O_3	CO	Batch	31866	100	180	1	1	Present work
Photo-induced CO_2 to CO	In_2O_{3-x} nanosheets	CO	Batch	103210	100	- (no external heating)	1	Not given	[10]
	Black In_2O_{3-x}/In_2O_3	CO	Batch	23882.75	100	- (no external heating)	1	2.1	[11]
	C-In_2O_{3-x}-3	CO	Batch	123600	100	- (no external heating)	1	Not given	[12]
	2% Ni-$LaInO_3$	CO	Flow	26280[a]	100	- (no external heating)	4	1	[13]
	Cs-promoted In_2O_3	CO	Flow	28000	100	- (no external heating)	4	1	[14]

	$In_2O_{3-x}(OH)_y@Nb_2O_5$	CO	Batch	1400	100	- (no external heating)	1	1.86	[15]
	$ntTiO_2@ncTiO_2@ncIn_2O_{3-x}(OH)_y$	CO	Batch	81000	100	- (no external heating)	5	1.24	[16]
	$In_2O_{3-x}(OH)_y$/SiNW	CO	Batch	22.0	100	- (no external heating)	1	2	[17]
	C-In_2O_3	CO	Flow	8510	100	- (no external heating)	4	1	[33]
	V-In_2O_3	CO	Batch	21280	100	- (no external heating)	1	1	Present work
Photo-induced or Photothermal CO_2 to CH_3OH	Ru/In_2O_3	MeOH [c]	Flow	280.4	18	275	3	1	[18]
	1.0% $Bi_xIn_{2-x}O_3$	MeOH [c]	Flow	158	14.68	230	3	1	[19]
	$In_2O_{3-x}(OH)_y$	MeOH [c]	Flow	97.3	50	250	3	1	[20]
	rh-$In_2O_{3-x}(OH)_y$	MeOH [c]	Flow	180	13	270	3	1	[21]
	rh/c-$In_2O_{3-x}(OH)_y$	MeOH [c]	Flow	92	7.6	270	3	1	[22]
	Black In_2O_3	MeOH [c]	Batch	31.2	36.7	- (no external heating)	3	2.1	[23]
	Black In_2O_3	MeOH [c]	Flow	6.48	33.2	250	1	1	[23]
	V-In_2O_3	MeOH [c]	Batch	204.54	20.09	- (no external heating)	3	1	Present work

[a] Calculated from given data;

[b] Mixing with minor methane;

[c] Mixing with CO

It is noteworthy that the activity data listed in the table are difficult to compare fairly due to the varying reaction conditions across different studies. Higher temperatures or pressures often enhance catalytic activity, while increased hydrogen ratios or elevated temperatures may improve selectivity toward high-value products. As shown in the table, the sample in this work demonstrates competitive activity and product selectivity under easily achievable reaction conditions.

Tab. S3 Infrared Band Assignments of the Surface Species.

Surface species	Wavenumber (cm^{-1})	Literature value (cm^{-1})
In-OH	3575	3554[29], 3550[28]
	3663	3650[29], ~3700[28]
	1240	1220[28], 1100-1200[11]
In-H	1640	1631[28], 1640[29]
	1404	1400[28], 1426[29], 1407[30]
HOCO-	1540	ν_{as}(OCO), 1555[24], 1567[25]
	1375	ν_{s}(OCO), 1370[24], 1360[26], 1359[25]
	2980	δ(CH) + ν_{as}(OCO), 2975[27], 2965[25]
	2875	ν(CH), 2885–2895[27], 2872[25]

References

1. W. Wei, Z. Wei, R. Li, Z. Li, R. Shi, S. Ouyang, Y. Qi, D. L. Philips, H. Yuan, *Nature Communications*, 2022, **13**, 3199.
2. Y. Dong, K. K. Ghuman, R. Popescu, P. N. Duchesne, W. Zhou, J. Y. Y. Loh, F. M. Ali, J. Jia, D. Wang, X. Mu, C. Kuebel, L. Wang, L. He, M. Ghoussoub, Q. Wang, T. E. Wood, L. M. Reyes, P. Zhang, N. P. Kherani, C. V. Singh, G. A. Ozin, *Advanced Science*, 2018, **5**, 1700732.
3. N. T. Nguyen, T. Yan, L. Wang, J. Y. Y. Loh, P. N. Duchesne, C. Mao, P.-C. Li, F. M. Ali, M. Xia, M. Ghoussoub, N. P. Kherani, Z.-H. Lu, G. A. Ozin, *Small*, **2020**, 16, 2005754.
4. L. B. Hoch, T. E. Wood, P. G. O'Brien, K. Liao, L. M. Reyes, C. A. Mims, G. A. Ozin, *Advanced Science*, 2014, **1**, 1400013.
5. K. K. Ghuman, T. E. Wood, L. B. Hoch, C. A. Mims, G. A. Ozin, C. V. Singh, *Physical Chemistry Chemical Physics*, 2015, **17**, 14623.
6. L. Hurtado, A. Mohan, U. Ulmer, R. Natividad, A. A. Tountas, W. Sun, L. Wang, B. Kim, M. M. Sain, G. A. Ozin, *Chemical Engineering Journal*, 2022, **435**, 134864.
7. L. B. Hoch, L. He, Q. Qiao, K. Liao, L. M. Reyes, Y. Zhu, G. A. Ozin, *Chemistry of Materials*, 2016, **28**, 4160.
8. L. He, T. E. Wood, B. Wu, Y. Dong, L. B. Hoch, L. M. Reyes, D. Wang, C. Kuebel, C. Qian, J. Jia, K. Liao, P. G. O'Brien, A. Sandhel, J. Y. Y. Loh, P. Szymanski, N. P. Kherani, T. C. Sum, C. A. Mims, G. A. Ozin, *Acs Nano*, 2016, **10**, 5578.
9. J. Y. Y. Loh, M. Shayegannia, N. P. Kherani, *Applied Catalysis B-Environmental*, 2021, **282**, 119555.
10. Y. H. Qi, L. Z. Song, S. X. Ouyang, X. C. Liang, S. B. Ning, Q. Q. Zhang, J. H. Ye, *Advanced Materials*, 2020, **32**, 1903915.
11. L. Wang, Y. Dong, T. Yan, Z. Hu, F. M. Ali, D. M. Meira, P. N. Duchesne, J. Y. Y. Loh, C. Qiu, E. E. Storey, Y. Xu, W. Sun, M. Ghoussoub, N. P. Kherani, A. S. Helmy, G. A. Ozin, *Nature Communications*, 2020, **11**, 2432.
12. Y. H. Qi, J. W. Jiang, X. C. Liang, S. X. Ouyang, W. B. Mi, S. B. Ning, L. Zhao, J. H. Ye, *Advanced Functional Materials*, 2021, **31**, 2100908.
13. J. Yu, A. Muhetaer, X. Gao, Z. Zhang, Y. Yang, Q. Li, L. Chen, H. Liu, D. Xu, *Angewandte Chemie-International Edition*, 2023, **62**, 202303135.
14. X. Wang, A. Rendon-Patino, J. M. R. Gallo, D. Mateo, J. Gascon, *Journal of Materials Chemistry A* 2024, **12**, 23541.

15. H. Wang, J. Jia, L. Wang, K. Butler, R. Song, G. Casillas, L. He, N. P. Kherani, D. D. Perovic, L. Jing, A. Walsh, R. Dittmeyer, G. A. Ozin, *Advanced Science*, 2019, **6**, 1902170.
16. N. T. Nguyen, M. K. Xia, P. N. Duchesne, L. Wang, C. L. Mao, F. M. Ali, T. J. Yan, P. C. Li, Z. H. Lu, G. A. Ozin, *Nano Letters*, 2021, **21**, 1311.
17. L. B. Hoch, P. G. O'Brien, F. M. Ali, A. Sandhel, D. D. Perovic, C. A. Mims, G. A. Ozin, *Acs Nano*, 2016, **10**, 9017.
18. B. Deng, H. Song, Q. Wang, J. Hong, S. Song, Y. Zhang, K. Peng, H. Zhang, T. Kako, J. Ye, *Applied Catalysis B-Environmental*, 2023, **327**, 122471.
19. T. J. Yan, N. Li, L. L. Wang, W. G. Ran, P. N. Duchesne, L. L. Wan, N. T. Nguyen, L. Wang, M. K. Xia, G. A. Ozin, *Nature Communications*, 2020, **11**, 6095.
20. L. Wang, M. Ghoussoub, H. Wang, Y. Shao, W. Sun, A. A. Tountas, T. E. Wood, H. Li, J. Y. Y. Loh, Y. C. Dong, M. K. Xia, Y. Li, S. H. Wang, J. Jia, C. Y. Qiu, C. X. Qian, N. P. Kherani, L. He, X. H. Zhang, G. A. Ozin, *Joule*, 2018, **2**, 1369.
21. T. J. Yan, L. Wang, Y. Liang, M. Makaremi, T. E. Wood, Y. Dai, B. B. Huang, F. M. Ali, Y. C. Dong, G. A. Ozin, *Nature Communications*, 2019, **10**, 2521.
22. T. J. Yan, N. Li, L. L. Wang, Q. Liu, F. M. Ali, L. Wang, Y. F. Xu, Y. Liang, Y. Dai, B. B. Huang, J. M. You, G. A. Ozin, *Energy & Environmental Science*, 2020, **13**, 3054.
23. Z. S. Zhang, C. L. Mao, D. M. Meira, P. N. Duchesne, A. A. Tountas, Z. Li, C. Y. Qiu, S. L. Tang, R. Song, X. Ding, J. C. Sun, J. F. Yu, J. Y. Howe, W. G. Tu, L. Wang, G. A. Ozin, *Nature Communications*, 2022, **13**, 1512.
24. T. Tagawa, N. Nomura, M. Shimakage, S. Goto, *Research on Chemical Intermediates*, 1995, **21**, 193.
25. S. Kattel, B. Yan, Y. Yang, J. G. Chen, P. Liu, *Journal of the American Chemical Society*, 2016, **138**, 12440.
26. M. Y. He, J. M. White, J. G. Ekerdt, *Journal of Molecular Catalysis*, 1985, **30**, 415.
27. E. Guglielminotti, *Langmuir*, 1990, **6**, 1455.
28. L. Wang, T. J. Yan, R. Song, W. Sun, Y. C. Dong, J. L. Guo, Z. Z. Zhang, X. X. Wang, G. A. Ozin, *Angewandte Chemie-International Edition*, 2019, **58**, 9501.
29. Z. Lu, Y. F. Xu, Z. S. Zhang, J. C. Sun, X. Ding, W. Sun, W. G. Tu, Y. Zhou, Y. F. Yao, G. A. Ozin, L. Wang, Z. G. Zou, *Journal of the American Chemical Society*, 2023, **145**, 26052.
30. L. Andrews, X. F. Wang, *Angewandte Chemie-International Edition*, 2004, **43**, 1706.

31. M. A. O. Fulin, D. A. I. Chunhua, P. Bingcheng, C. A. O. Jian, F. E. I. Zhenghao, *Applied Chemical Industry*, 2007, **36**, 446.
32. C. Qin, Y. Zhang, Y. Wang, Y. Zhang, J. Cao, *Acs Applied Nano Materials*, 2023, **6**, 5635.
33. J. Zhou, X. Zhao, L. Huang, Y. Zhang, X. Zhou, Y. Fan, S. Mo, Y. Sun, Q. Xie, D. Ye, *Separation and Purification Technology* 2025, **355**, 129672.